

Shear dispersion in the turbulent atmospheric boundary layer

J. G. Esler* and H. M. Ramli

Department of Mathematics, University College London, UK

*Correspondence to: J. G. Esler, Department of Mathematics, University College London, Gower Street, London WC1E 6BT, UK. E-mail: j.g.esler@ucl.ac.uk

The problem of shear dispersion in the atmospheric boundary layer (ABL) is revisited. The aim is to improve understanding of how and why the behaviour of state-of-the-art ‘random flight’ Lagrangian particle dispersion models (RFMs) can differ from that of simpler ‘random displacement’ models (RDMs or eddy diffusivity models). First an asymptotic analysis is used to obtain a formula, valid for quite general profiles of turbulent statistics and the mean wind, for the effective horizontal diffusivity of a tracer in the ABL. Second, with ‘poison gas release’ problems in mind, a large-deviation approach is used to understand in greater detail the behaviour of the concentration in the tails of the distribution. Results are verified by solving the RFM equations numerically for a large ensemble of particles. Turbulent statistics relevant to stable and neutral boundary-layer conditions are considered, as is the effect of non-uniqueness in the RFM equations. The importance of three-dimensional effects such as the effect of an Ekman spiral in the mean wind are then considered, and criteria determining whether plume widths are controlled by direct horizontal diffusion or by secondary shear dispersion effects are obtained. Finally, a quantitative account of ‘plume bending’ in the stable ABL is presented.

Key Words: stochastic Lagrangian models; effective diffusivity; large-deviation theory

Received 17 November 2016; Revised 11 March 2017; Accepted 16 March 2017; Published online in Wiley Online Library 24 May 2017

1. Introduction

Shear dispersion, sometimes Taylor or Taylor–Aris dispersion (Taylor, 1953; Aris, 1956), is a fundamental process in fluid dynamics. In shear dispersion problems the diffusion of a tracer in the along-flow direction of a unidirectional but non-uniform flow is found to be controlled, not by the direct diffusion acting in the along-flow direction, but by diffusion in the across-flow direction acting in concert with the shear in the flow. Counter-intuitively, the dominant term in the effective diffusivity in the along-flow direction is found to be *inversely* proportional to the across-flow diffusivity. This is because, when the across-flow diffusivity is weak, individual fluid particles experience coherent differential advection by the shear flow for relatively long periods, leading to particles becoming widely dispersed in the along-flow direction. By contrast, in the limit of strong across-flow diffusivity, particles experience only (non-dispersive) advection by the mean flow.

The relevance of shear dispersion to atmospheric boundary layer (ABL) flows has long been recognised. In a classic paper Saffman (1962) derived analytical solutions for two idealized problems. In the first problem, vertical diffusion is assumed uniform up to a fixed boundary-layer height, where a no-flux boundary condition is imposed. In the second problem, the vertical diffusion is uniform and unbounded with height. Subsequent researchers (e.g. Smith, 1965, 2005; Tyldesley and Wallington, 1965; Taylor, 1982) have mainly focused on the paradigm presented by the second solution, which is relevant

to the early stages of a tracer release problem in which a near-Gaussian tracer plume or puff spreads freely in the vertical, interacting only with the surface. The present work, by contrast, is motivated in part by the desire to understand shear dispersion in state-of-the-art Lagrangian dispersion models such as FLEXPART (Stohl *et al.*, 2005) and NAME (Jones *et al.*, 2007). In these models a no-flux boundary condition is imposed at the top of ABL as in Saffman’s first problem above, and corresponds physically to the trapping of fluid particles within the ABL by a horizontal interface with high stratification (i.e. an inversion layer).

The set-up of Saffman’s first problem is illustrated in Figure 1, which shows scatterplots of an ensemble of trajectories in stable ABL conditions, integrated using a Lagrangian model to be described in detail below. Following a point release of tracer, here at half the ABL height h , there is a time period of the order of hu_*^{-1} , where u_* is the surface friction velocity (equal to $\sqrt{\tau_0/\rho}$ where τ_0 is the Reynolds stress of the mean wind at the surface), over which particles become homogenised in the vertical (Figures 1(a) and (b)). After this homogenization period, shear dispersion over the depth of the ABL ensues. In the ABL, hu_*^{-1} is typically of the order of tens of minutes. Consequently Saffman’s first problem has practical relevance for understanding the horizontal dispersion of tracers in the ABL over periods of a few hours. Saffman’s main result for the one-dimensional problem, for an ABL with a height-dependent isotropic diffusivity $\kappa(z)$ and shear flow $u(z)$, is as follows. Denoting the vertical mean taken over the depth of the ABL by angle brackets, the vertical mean concentration $\langle c \rangle(x, t)$

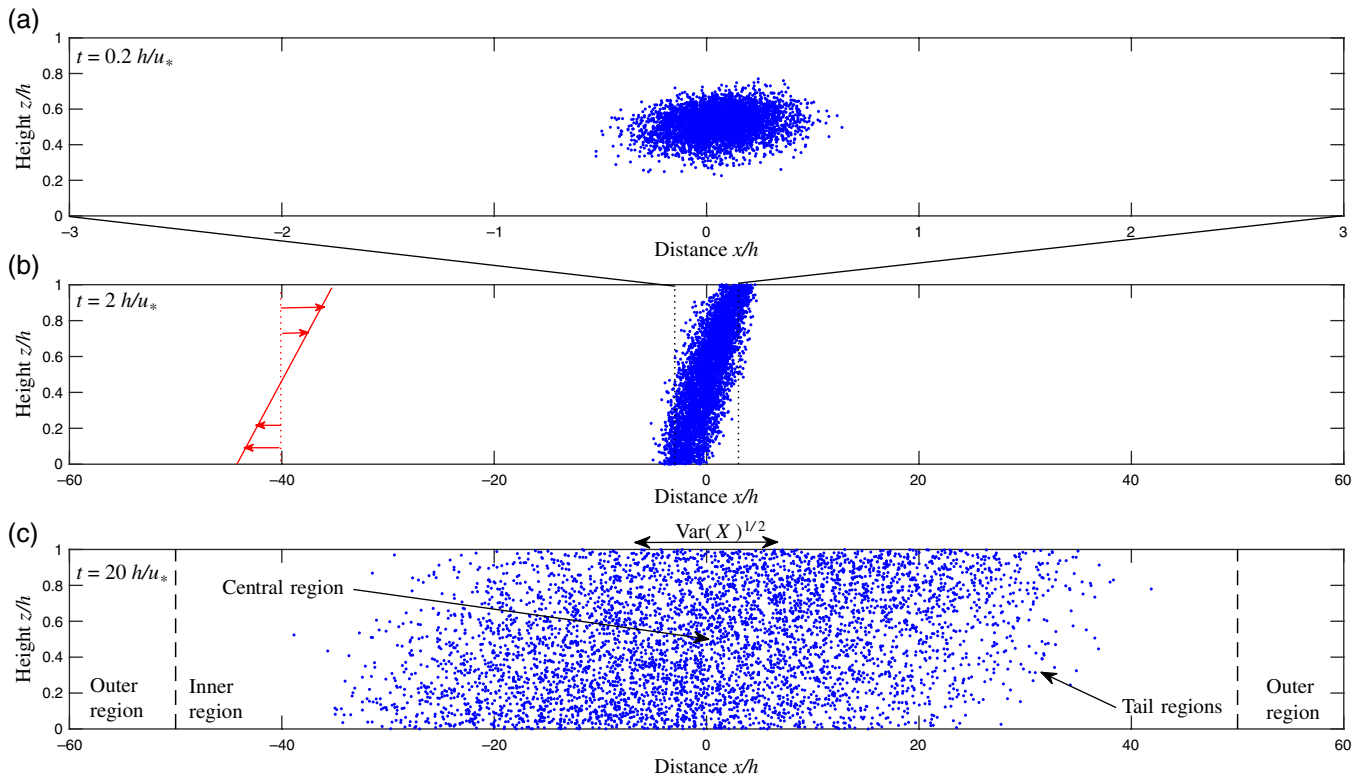


Figure 1. Scatterplots of an ensemble of $N = 5000$ trajectories, following a point release at $(X, Z) = (0, 0.5)$, as simulated by the RFM (3) in the stable ABL case: (a) early-time dispersion $t = 0.2 hu_*^{-1}$, (b) when particles have become well-mixed in the vertical by time $t = 2 hu_*^{-1}$, and (c) at late time ($t = 20 hu_*^{-1}$) when shear dispersion is well-established. A key measure of shear dispersion, the standard deviation $\text{Var}(X)^{1/2} \approx (2\kappa_{\text{eff}}t)^{1/2}$, is shown for reference. [Colour figure can be viewed at wileyonlinelibrary.com].

evolves according to the advection-diffusion equation

$$\partial_t \langle c \rangle + \langle u \rangle \partial_x \langle c \rangle = \kappa_{\text{eff}} \partial_{xx}^2 \langle c \rangle. \quad (1)$$

Results of the form (1) are generic to a wide range of tracer dispersion problems (e.g. Majda and Kramer, 1999) and can be found using the method of homogenization (Pavliotis and Stuart, 2007), as well as the method of moments used by Saffman. The effective diffusivity κ_{eff} in Saffman's problem is given by

$$\kappa_{\text{eff}} = \left\langle \frac{F^2}{\kappa} + \kappa \right\rangle, \quad \text{where } F(z) = \int_0^z \{u(\bar{z}) - \langle u \rangle\} d\bar{z}. \quad (2)$$

In practice κ_{eff} is usually dominated by the first term which, as anticipated by the discussion above, depends on the inverse of the diffusivity $\kappa(z)$.

The present work will re-examine the paradigm presented by Saffman's first problem. The aim is to better understand the shear dispersion process as it takes place in state-of-the-art particle dispersion models designed for the ABL (e.g. FLEXPART and NAME). Specifically, the following questions will be addressed:

1. Does κ_{eff} change significantly if random flight models (RFMs) are used instead of random displacement models (RDMs)? Both FLEXPART and NAME are RFMs, meaning that they model turbulent dispersion using stochastic processes that describe a turbulent velocity field with a realistic Lagrangian decorrelation time. However, the results of Saffman (1962) apply directly only to RDMs, which corresponds to both the limit of zero decorrelation time of the RFM (e.g. Rodean, 1996) and, equivalently, to the standard advection-diffusion model.
2. Is the large-deviation behaviour influenced by the type of model used? Large-deviation theory (Haynes and Vanneste, 2014) describes the evolution of the low concentrations seen in the tails of a spreading cloud of parcels, and can be important in estimating the time-scale on which a threshold concentration is first met at a given location

downstream, which might be important, for example, in a problem involving a toxic gas or aerosol release. It is not obvious *a priori* how concentrations in the tails will change if an RFM is used as opposed to an RDM.

3. Under realistic three-dimensional ABL conditions, what controls the horizontal effective diffusivity in the direction perpendicular to the principal direction of the wind shear? Under what conditions is shear dispersion due to wind curvature with height (e.g. in an Ekman layer) more important than direct horizontal turbulent diffusivity?

Questions 1–3 will be answered by comparing analytical, semi-analytical and numerical results. Note that the present work will focus on the late-time behaviour of ABL flows, leaving questions relating to the early-time corrections to the shear dispersion framework (e.g. Young and Jones, 1991; Camassa *et al.*, 2010) to a future work. In section 2, the RFM and RDM models are introduced, and the large-deviation approach to the RDM model is described, reviewing the results of Haynes and Vanneste (2014). In section 3, analytical results are presented for the effective diffusivity, and numerical results for the tracer decay rate at large distances which is controlled by the large-deviation rate function. Possible behaviours due to non-uniqueness of the RFM are then considered. Finally three-dimensional effects, e.g. due to an Ekman spiral in the mean wind, are investigated. Throughout section 3, results are compared with numerical calculations of large ensembles of tracer particles, using both the RFM and RDM where appropriate. The differences between two models are investigated in both stable and neutral conditions. Finally, in section 4, conclusions are drawn.

2. Model and background

2.1. The random flight model (RFM)

The RFM to be investigated is defined by the following set of stochastic differential equations, describing the time evolution of the position (X, Z) and eddy velocity (U, W) of a single fluid parcel

in a turbulent boundary layer with Gaussian velocity statistics:

$$\left. \begin{aligned} dU &= -\frac{U}{\tau_1} dt + \left(\frac{2\sigma_1^2}{\tau_1}\right)^{1/2} dB_1, \\ dW &= \left[-\frac{W}{\tau_2} + \frac{1}{2} \left\{ 1 + \left(\frac{W}{\sigma_2}\right)^2 \right\} \frac{d(\sigma_2^2)}{dz} \right] dt \\ &\quad + \left(\frac{2\sigma_2^2}{\tau_2}\right)^{1/2} dB_2, \\ dX &= (u + U) dt, \\ dZ &= W dt. \end{aligned} \right\} \quad (3)$$

Here (B_1, B_2) are Brownian (Wiener) processes. Throughout, stochastic variables (e.g. X, Z, U, W) will be denoted by capitals. The mean horizontal velocity profile is given by $u(z)$ and the turbulent statistics in the ABL are specified by the turbulent velocity scales $(\sigma_1(z), \sigma_2(z))$, and Lagrangian decorrelation times $(\tau_1(z), \tau_2(z))$, where the subscripts 1 and 2 refer to the horizontal and vertical directions respectively. Three profiles used throughout this work, corresponding to an ABL with idealized (constant) statistics, and to stable and neutral ABL conditions, are described in Appendix A.

For the purposes of this work, the equation set (3) will be interpreted as being non-dimensional, with the boundary-layer height h , the surface friction velocity u_* and hu_*^{-1} as scales for velocity, length and time respectively. Under this scaling, no explicit non-dimensional parameters appear in the problem. Note also that the mean velocity profile $u(z)$ will typically have a large magnitude (measured in units of u_*), i.e. the implicit parameter

$$\mathcal{U} = u_{\max} - u_{\min}, \quad (4)$$

where u_{\max} and u_{\min} are the maximum and minimum values of $u(z)$ respectively, is typically $O(10)$ or greater. Finally, without loss of generality, the vertical mean of $u(z)$ will be taken to be zero, i.e. we will work in the frame following the mean position of the ensemble of trajectories.

Physically, it is easy to understand most of the terms in (3). The equations for (X, Z) are standard trajectory equations, whereas those for (U, W) resemble Ornstein–Uhlenbeck processes, or random walks in quadratic potential wells, which in spatially homogeneous turbulence would result in (U, W) having ‘red noise’ frequency spectra. The additional term in the W -equation is necessary for the model to be ‘well-mixed’ in the sense of Thomson (1987), as will be discussed below. Equation (3) is essentially that used in FLEXPART (Stohl *et al.*, 2005) and NAME (Jones *et al.*, 2007) to model dispersion in the ABL. Following these models, reflection boundary conditions are used at the model boundaries at $z = 0, 1$. Physically, reflection at the boundary-layer top ($z = 1$) is (at least partially) justified when the ABL has locally developed a sharp gradient in buoyancy, forming an interface across which there is a large decrease in the intensity of turbulence. Wilson and Flesch (1993) and Thomson *et al.* (1997) have discussion, including the possibility of more sophisticated boundary conditions.

Following Rodean (1996) it is easier to work with scaled velocities $(\Lambda, \Omega) = (U/\sigma_1(Z), W/\sigma_2(Z))$ which, following application of Itô’s lemma, satisfy

$$\left. \begin{aligned} d\Lambda &= -\frac{\Lambda}{\tau_1} dt + \left(\frac{2}{\tau_1}\right)^{1/2} dB_1, \\ d\Omega &= \left(-\frac{\Omega}{\tau_2} + \frac{d\sigma_2}{dz}\right) dt + \left(\frac{2}{\tau_2}\right)^{1/2} dB_2, \\ dX &= (u + \Lambda\sigma_1) dt, \\ dZ &= \Omega\sigma_2 dt. \end{aligned} \right\} \quad (5)$$

A complementary approach to systems of stochastic differential equations such as (5) is to consider the corresponding

Fokker–Planck equation (FPE) for the time-evolution of the joint probability density $p(x, z, \lambda, \omega, t)$ of the stochastic variables (X, Z, Λ, Ω) . Following the standard procedure, outlined for example in section 3.4.1 of Gardiner (2009), the FPE of (5) is found to be

$$\begin{aligned} p_t + \{(u + \lambda\sigma_1)p\}_x + (\omega\sigma_2 p)_z + (\sigma_2' p)_\omega \\ = \tau_1^{-1} (p_\lambda + \lambda p)_\lambda + \tau_2^{-1} (p_\omega + \omega p)_\omega. \end{aligned} \quad (6)$$

Here subscripts denote partial derivatives and $\sigma_2' \equiv d\sigma_2/dz$. The reflecting boundary conditions at $z = z_b$ become

$$p(x, z_b, \lambda, \omega) = p(x, z_b, \lambda, -\omega) \quad \text{for } z_b = 0, 1. \quad (7)$$

Most of our results below will be based on analysis of (6)–(7).

The stationary density

$$p_e = \text{constant} \times \exp\left\{-\frac{1}{2}(\lambda^2 + \omega^2)\right\} \quad (8)$$

is the steady solution of (6). The solution p_e or, in the language of probability theory, the *invariant measure* of (5), is interpreted physically as the distribution of particles in the background atmosphere in position–velocity space. The ‘well-mixed’ criterion of Thomson (1987) corresponds to ensuring that the invariant measure of the system of stochastic differential equations being solved corresponds to a notional, pre-specified distribution p_e , which in general is determined by the statistics of the background atmosphere.

2.2. The random displacement model (RDM) and its large-deviation behaviour

It is well-known (e.g. section 6.3 of Rodean, 1996) that the RFM (5) can be approximated by the simpler RDM in the distinguished limit of short decorrelation time $\tau_i \rightarrow 0$ and large velocity fluctuations $\sigma_i \rightarrow \infty$, in which $\sigma_i^2 \tau_i = \kappa_i$ (here $i = 1, 2$) is finite and non-zero. The equation set (5) can in this case be replaced by

$$\begin{aligned} dX &= u dt + (2\kappa_1)^{1/2} dB_1, \\ dZ &= \kappa_2' dt + (2\kappa_2)^{1/2} dB_2, \end{aligned} \quad (9)$$

where $\kappa_2' \equiv d\kappa_2/dz$. The FPE of (9), which is the equivalent of (6) for the RDM, is simply the advection–diffusion equation

$$c_t + u c_x = \kappa_1 c_{xx} + (\kappa_2 c_z)_z, \quad (10)$$

where we have identified the joint pdf of (X, Z) in (9) with the particle concentration $c(x, z, t)$ (in general, these can differ by a multiplicative constant). The effective diffusivity result, generalizing (1), can be obtained from (10) by applying the method of moments (following Saffman, 1962), or the method of homogenization (e.g. Pavliotis and Stuart, 2007). Its exact form is given in section 3.1 below.

The effective diffusivity paradigm of (1) does not give the full picture of the long-time dispersion of tracer particles according to (9). In certain problems, for example the point release of a highly toxic substance, the quantity of interest can be the time taken for the tracer concentration to first reach a given (low) threshold at a particular location. The evolution of the relatively low concentrations in the tails of the spreading cloud of particles are described mathematically by large-deviation theory. Recently, Haynes and Vanneste (2014) considered the large-deviation behaviour of (10), focusing on classic Taylor–Aris dispersion problems (Couette flow, plane Poiseuille flow and pipe Poiseuille flow). The main point is that, while in the central region (where $x^2/t \sim O(1)$), the evolution of $\langle c \rangle$ is well-described by the effective diffusivity model (1); in the tails of the distribution

(where $x/t \sim O(1)$) the concentration $c(x, z, t)$ can be shown to satisfy

$$c(x, z, t) \sim t^{-1/2} \phi(z, \xi) e^{-t g(\xi)}, \quad \text{where } \xi = x/t. \quad (11)$$

Here $\phi(z, \xi)$, which is determined by solving a family of eigenvalue problems parametrized by ξ , gives the local vertical structure of the tracer profile. In the central region ($\xi \approx 0$), where the tracer is well-mixed in the vertical, it turns out that $\phi(z, 0) = 1$. The effective diffusivity result for the central region can be recovered from the leading term in a Maclaurin expansion of the so-called rate function $g(\xi)$, which is given by $g''(0)\xi^2/2$. Here, $g(0) = 0$ follows from conservation of mass, and $g'(0) = 0$ from the fact we are working in the frame of the mean wind. It follows, by comparison with the well-known ‘heat kernel’ solution of (1), that $\kappa_{\text{eff}} = 1/(2g''(0))$.

In the tail regions, by contrast, according to (11) the decay rate of the tracer is controlled by the rate function $g(\xi)$. If the effective diffusivity model were valid everywhere, then the rate function would be everywhere equal to its quadratic approximation $g_0(\xi) = \xi^2/4\kappa_{\text{eff}}$. However, the calculations of Haynes and Vanneste (2014) revealed that typically $g(\xi) \gtrsim g_0(\xi)$, indicating that tracer concentrations fall off much more rapidly in the tail regions than predicted by the effective diffusivity model. In fact there are two distinct regimes: an inner region for which $\xi \in (u_{\text{min}}, u_{\text{max}})$ (containing the central region) and an outer region $\xi > u_{\text{max}}$ and $\xi < u_{\text{min}}$. The regions are distinct because particles can arrive at any location in the inner region under the influence of horizontal advection alone (e.g. by remaining at a level near that of the maximum or minimum velocity). By contrast, a particle can only reach a location in the outer region by a favourable combination of horizontal advection and horizontal diffusion. The transition between the two regimes is evident as $g(\xi)$ is typically found to increase very rapidly from the inner to the outer region. Tracer concentrations are consequently very low in the outer region, where they are controlled by the direct horizontal diffusivity. One of our main aims below is to determine the extent to which the rate function $g(\xi)$ depends on whether the RFM or RDM is used.

3. Results

3.1. Effective diffusivity in the RFM

The main purpose of this section is to use an asymptotic approach to calculate the effective horizontal diffusivity for particles released in the RFM. To effect this analysis, two parameters are introduced. First $\varepsilon = h/L$ is the ratio of the ABL depth to the horizontal length-scale of the cloud of particles. Second, $\delta = u_* \tau/h$ is the ratio of a typical Lagrangian decorrelation time τ to the reference time-scale hu_*^{-1} .

The most interesting tractable regime appears to be $\varepsilon \ll \delta \ll 1$. Enforcing $\varepsilon \ll \delta$ corresponds to focusing only on the late-time behaviour for which the diffusive approximation applies. As explained in Haynes and Vanneste (2014), next-order effects in ε , which could be recovered here by considering the distinguished limit $\varepsilon \sim \delta \ll 1$, result in the diffusion equation being augmented with higher derivative terms (e.g. $\partial_x^3 \langle c \rangle$), which are important only at early times. Such an augmented diffusion equation does not preserve positivity, and hence is not very useful in practice. It is a property of empirical profiles of turbulent statistics that $\delta \lesssim 1$, which justifies consideration of $\delta \ll 1$.

Based on these insights, we seek solutions of (6) of the form $p = p(\bar{x}, z, \lambda, \omega, \bar{t})$ where \bar{x} and \bar{t} are long time and space scales satisfying

$$\bar{x} = \varepsilon x, \quad \bar{t} = \varepsilon^2 t. \quad (12)$$

Further, the turbulent statistics σ_i and τ_i are rescaled as follows

$$\sigma_i = \delta^{-1} \bar{\sigma}_i, \quad \tau_i = \delta^2 \bar{\tau}_i. \quad (13)$$

Notice that this scaling preserves the relationship with the diffusivity, since $\sigma_i^2 \tau_i = \bar{\sigma}_i^2 \bar{\tau}_i = \kappa_i$.

The primary expansion in ε , relative to which δ is treated as finite, is

$$p = \sum_{j=0}^{\infty} \varepsilon^j p_j(\bar{x}, z, \lambda, \omega, \bar{t}). \quad (14)$$

Inserting this expansion into (6), at leading order in ε ,

$$\mathcal{L}p_0 = \delta (\omega \bar{\sigma}_2 p_0)_z + \delta (\bar{\sigma}'_2 p_0)_\omega, \quad (15)$$

where the linear operator \mathcal{L} acts on functions $f(\lambda, \omega, z)$ as follows:

$$\mathcal{L}f \equiv \bar{\tau}_1^{-1} (f_\lambda + \lambda f)_\lambda + \bar{\tau}_2^{-1} (f_\omega + \omega f)_\omega. \quad (16)$$

The leading-order equation (15) has the ‘well-mixed’ solution

$$p_0 = P(\bar{x}, \bar{t}) \exp \left\{ -\frac{1}{2} (\lambda^2 + \omega^2) \right\}, \quad (17)$$

where $P(\bar{x}, \bar{t})$ is at this order an undetermined function of the ‘long’ space and time variables (\bar{x}, \bar{t}) .

At $O(\varepsilon)$ in the expansion

$$\mathcal{L}p_1 - \delta (\omega \bar{\sigma}_2 p_1)_z - \delta (\bar{\sigma}'_2 p_1)_\omega = \delta^2 u p_{0\bar{x}} + \delta \lambda \bar{\sigma}_1 p_{0\bar{x}}. \quad (18)$$

To proceed, a particular integral needs to be found for (18). A solution can be sought based on a Hermite polynomial (Gram–Charlier type A) expansion

$$p_1 = \sum_{k=0}^{\infty} \text{He}_k(\omega) \left\{ C_k(z) + \lambda D_k(z) \right\} \times P_{\bar{x}}(\bar{x}, \bar{t}) \exp \left\{ -\frac{1}{2} (\lambda^2 + \omega^2) \right\}. \quad (19)$$

The probabilists’ Hermite polynomials $\text{He}_k(\cdot)$ are defined in Appendix B1, where their relevant properties are listed. Solving for p_1 involves determining the sequences of functions $\{C_k(z)\}$ and $\{D_k(z)\}$. In Appendix B2, asymptotic approximations to the leading terms in these sequences are evaluated, and it is shown that $C_k \sim O(\delta^k)$ and $D_k \sim O(\delta^{k+1})$. Note that the full solution for p_1 also includes a complementary function, similar to the well-mixed solution for p_0 given above, but this can be set to zero without loss of generality in order to define a unique separation between the various orders in the expansion (14).

It is at $O(\varepsilon^2)$ in the expansion that the effective diffusivity can be calculated. The equation for p_2 is

$$\mathcal{L}p_2 - \delta (\omega \bar{\sigma}_2 p_2)_z - \delta (\bar{\sigma}'_2 p_2)_\omega = \delta^2 p_{0\bar{t}} + \delta^2 u p_{1\bar{x}} + \delta \lambda \bar{\sigma}_1 p_{1\bar{x}}. \quad (20)$$

At this order it is not necessary to solve explicitly for p_2 . Instead, the *solvability condition* of (20) can be used to obtain the effective horizontal diffusivity. The solvability condition arises because the integral of the left-hand side of (20), over the domain $\{D : (\lambda, \omega) \in \mathbb{R}^2, z \in [0, 1]\}$ is evidently zero. The corresponding integral over the right-hand side must also be zero, i.e.

$$\int_D (p_{0\bar{t}} + u p_{1\bar{x}} + \delta^{-1} \lambda \bar{\sigma}_1 p_{1\bar{x}}) dz d\lambda d\omega = 0. \quad (21)$$

Evaluating this integral, and using the orthogonality properties of the Hermite polynomials, the one-dimensional diffusion equation is obtained

$$P_{\bar{t}} = \kappa_{\text{eff}} P_{\bar{x}\bar{x}}, \quad (22)$$

where the effective diffusivity is given by

$$\begin{aligned} \kappa_{\text{eff}} &= -\langle uC_0 + \delta^{-1}\bar{\sigma}_1 D_0 \rangle \\ &= \langle FC'_0 - \delta^{-1}\bar{\sigma}_1 D_0 \rangle \\ &= \kappa_{\text{eff}}^{(1)} + \kappa_{\text{eff}}^{(2)}, \end{aligned} \tag{23}$$

where, as above, angle brackets denote the vertical average of a quantity over the boundary layer, and $F(z)$ is the integral of the mean wind profile as in (2). In direct analogy with Saffman’s result (2), the two terms $\kappa_{\text{eff}}^{(1)}$ and $\kappa_{\text{eff}}^{(2)}$ refer to the two separate terms in the vertical average, with the much larger term $\kappa_{\text{eff}}^{(1)}$ being due to shear dispersion, and the smaller term $\kappa_{\text{eff}}^{(2)}$ being due to direct horizontal diffusion.

It is evident from (23) that only C'_0 and D_0 are needed to calculate κ_{eff} , which guides our approach to solving (18) in Appendix B2. There, it is shown that, approximately,

$$\kappa_{\text{eff}}^{(1)} = \left\langle \frac{F^2}{\kappa_2} + \kappa_2 \left(\frac{F}{\sigma_2} \right)' \right\rangle - \frac{\kappa_2}{2} \left\langle \frac{\kappa_2}{\sigma_2} \left(\frac{F}{\sigma_2} \right)' \right\rangle^2. \tag{24}$$

Equation (24) can be interpreted as an expansion in δ^2 , including three terms of $O(1)$, $O(\delta^2)$ and $O(\delta^4)$ respectively, and with terms of $O(\delta^6)$ neglected. The leading term is identical to the first term in Saffman’s result (2), with the remaining terms giving the corrections due to the finite decorrelation times in the RFM (3). It is notable that the dominant correction, given by the second term in (24), is always positive. Consequently, at least for small δ , the effective horizontal diffusivity will always be greater in the RFM compared to its RDM limit.

Following a similar procedure, the direct diffusivity (here correct to the first two terms) is found to be

$$\kappa_{\text{eff}}^{(2)} = \left\langle \kappa_1 + \frac{\kappa_2 \tau_1}{\tau_1 + \tau_2} \left(\frac{\kappa_1}{\sigma_1} \right)' \right\rangle. \tag{25}$$

Once again, the leading correction term is positive definite, showing that shear dispersion is always increased in the RFM compared with the RDM.

An important point is that the expansion in δ^2 underpinning the results (24)–(25) is a singular rather than a regular perturbation expansion, as is commonly found in multiple scales expansions. This means that the resulting series in (24)–(25) will be divergent, and as a result the optimal agreement between the series expansions and the full model at finite δ will be obtained by truncating the series at a finite number of terms.

3.2. Numerical calculation of κ_{eff} in the RFM

The validity and accuracy of the results (24)–(25) can be tested by comparison with direct integration of the RFM (3). It is not obvious *a priori* that (24)–(25) will be accurate or relevant, because they are formally valid only for $\delta \ll 1$, and obviously δ takes a finite value for any physically realistic profile of ABL statistics.

Three profiles of turbulent statistics are tested in detail, corresponding to a simple idealized profile with constant τ_i and σ_i , a stable ABL and a neutral ABL respectively. Details of all three profiles are given in Appendix A. In each case a linear shear flow $u(z) = \mathcal{U}(z - 0.5)$ is used. (Recall: the velocity unit is the friction velocity u_* , and $\mathcal{U} = u_{\text{max}} - u_{\text{min}} \sim O(1 - 100)$ is typical of the observed ABL.) Here $\mathcal{U} = 5$ is used. A linear shear flow is chosen here primarily for analytical convenience (see section 3.5 below). However tests with more realistic wind profiles have yielded similar results.

Effective diffusivities in the RFM (3) are calculated based on the fact that

$$\kappa_{\text{eff}} = \lim_{t \rightarrow \infty} \frac{\text{Var}(X)}{2t}. \tag{26}$$

In practice, the RFM is run for a suitably long period (typically $50-100 hu_*^{-1}$), and a least-squares linear fit is then made to $\text{Var}(X)(t)$ for the later part of the integration period. Then κ_{eff} is obtained from the gradient of this fit, with error bars estimated by sub-sampling.

To create a robust test of (24)–(25), and better understand the limitations of the approach of section 3.1, a wider class of RFM models are introduced as follows. For each of the three profiles detailed in Table A1, a one-parameter of ‘interpolated’ RFM models is defined by the transformation:

$$\sigma_i \rightarrow \delta^{-1}\sigma_i, \quad \tau_i \rightarrow \delta^2\tau_i. \tag{27}$$

Here the ‘interpolating parameter’ δ has an analogous role to δ in the theory of section 3.1, which is formally valid only for models with $\delta \ll 1$. Specifically:

- $\delta = 0$: recovers the RDM limit.
- $0 < \delta < 1$: corresponds to a family of models with shorter decorrelation times (more ‘diffusive’ behaviour) than the observed ABL.
- $\delta = 1$: corresponds to the RFM with observed ABL statistics as in Table A1.
- $\delta > 1$: corresponds to a family of models with longer decorrelation times (more ‘ballistic’ behaviour) than the observed ABL.

Figure 2 shows a comparison between κ_{eff} calculated directly from RFM calculations (points with error bars) and from (24)–(25) (black curves). Results are obtained from integrations of the interpolated models with $0 \leq \delta \leq 2$, for idealized, stable and neutral ABL profiles respectively. Note that the $\delta = 0$ results are obtained by integrating (9) rather than (3). The results show that

- The three profiles (ideal, stable and neutral) have rather different values of κ_{eff} . The controlling factor in each case is the magnitude of the vertical diffusivity $\kappa_2(z)$ (relatively high in ideal, low in neutral), with the greatest sensitivity being to the value in the centre of the domain where F^2 is largest.
- The analytical results (24)–(25) remain accurate for $\delta \lesssim 1$ for all three profiles, and only at $\delta = 2$ begin to diverge significantly from the RFM calculations. The small- δ theory appears to be justified in practice.
- The difference in κ_{eff} between the physical RFMs ($\delta = 1$) and their RDM limit ($\delta = 0$) is rather small, in fact just 9.08, 2.74 and 0.76% for the ideal, stable and neutral profiles.

In summary, for flows with realistic ABL statistics, the modelled rate of shear dispersion is relatively unchanged if the RDM is used in place of the RFM. However this result, which applies to the central region only, does not tell us anything about dispersion in the tails which will be addressed next.

3.3. Dispersion in the tail regions

The above sections were concerned with dispersion in the central region, where $x^2/t \sim O(1)$. The results do not tell us anything about changes in the tail regions where $x/t \equiv \xi \sim O(1)$, which can be important if the key measurement is the time at which a tracer concentration first meets a fixed threshold, e.g. the ‘poison release’ scenario discussed above. Hence the following question is of interest: does the rate function $g(\xi)$, which controls the tracer decay rate in the tail regions, change significantly if the RFM is used in place of the RDM?

Haynes and Vanneste (2014) have calculated $g(\xi)$ for the RDM (via the advection–diffusion equation (10)), and here their method is adapted for the Fokker–Planck equation (6) corresponding to the RFM. A leading-order WKBJ-type solution of (6) is sought using the ansatz

$$p(x, z, \lambda, \omega, t) \sim t^{-1/2} \phi(z, \lambda, \omega, \xi) e^{-t g(\xi)}. \tag{28}$$

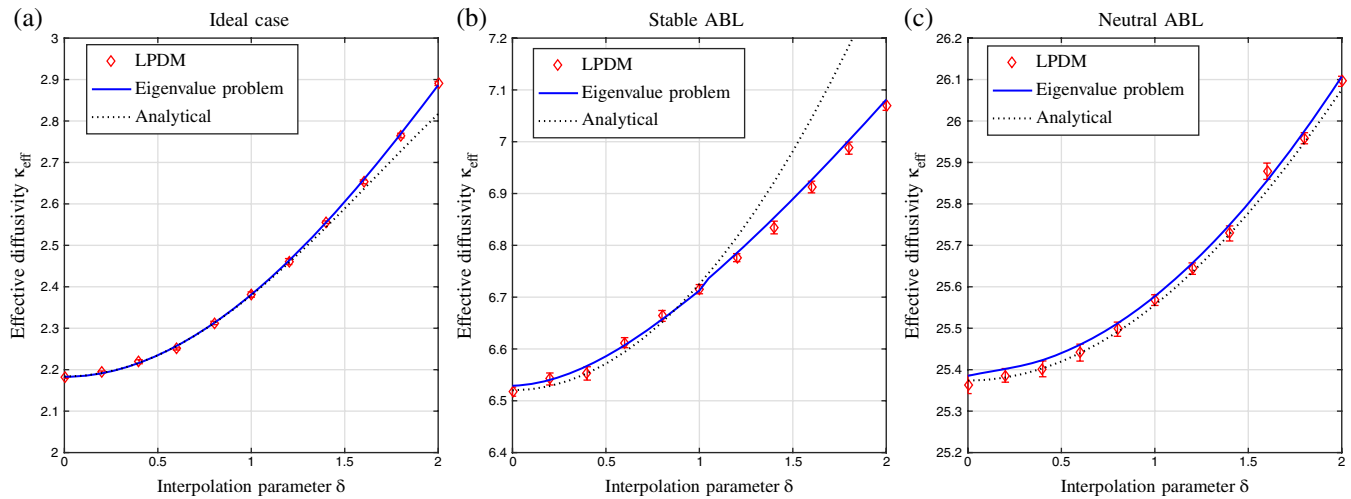


Figure 2. Effective diffusivity κ_{eff} in the ‘interpolated models’ derived from the three ABL flows –(a) idealized, (b) stable, (c) neutral – detailed in Table A1, as a function of the interpolation parameter δ . Note that $\delta = 0$ corresponds to the RDM limit, and $\delta = 1$ recovers the standard RFM. Points show κ_{eff} obtained from an ensemble of integrations of (3) using (26). The dotted curves show the analytical predictions ((24)–(25)), and the solid (blue online) curves show κ_{eff} obtained numerically from the eigenvalue problem ((29)–(30)). [Colour figure can be viewed at wileyonlinelibrary.com].

The function $\phi(z, \lambda, \omega, \xi)$ is found to be determined by a single-parameter family of eigenvalue problems

$$\mathcal{L}\phi + \{(u + \lambda\sigma_1)q\} \phi - (\omega\sigma_2\phi)_z - (\sigma'_2\phi)_\omega = f(q)\phi, \quad (29)$$

where \mathcal{L} is the linear operator defined in (16) with τ_i used in place of $\bar{\tau}_i$. The reflecting boundary conditions at $z = 0, 1$ are

$$\left. \begin{aligned} \phi(0, \lambda, \omega, \xi) &= \phi(0, \lambda, -\omega, \xi), \\ \phi(1, \lambda, \omega, \xi) &= \phi(1, \lambda, -\omega, \xi). \end{aligned} \right\} \quad (30)$$

The family of eigenvalue problems (29)–(30) are parametrized by $q = g'(\xi)$, in the sense that there is a one-to-one mapping between q and the ‘velocity’ of interest ξ . The lead eigenvalues $f(q)$ and the rate function $g(\xi)$ are related through the Legendre transform pair

$$\left. \begin{aligned} f(q) &= \sup_{\xi} \{q\xi - g(\xi)\}, \\ g(\xi) &= \sup_q \{\xi q - f(q)\}. \end{aligned} \right\} \quad (31)$$

Consequently, if the eigenvalue problem (29)–(30) is solved numerically for a range of values of q , the values of the principle eigenvalue $f(q)$ can be used to obtain $g(\xi)$ by (numerically) inverting the transform (31). In practice a nonlinear programming algorithm (MATLAB’s `fminsearch`) is used.

Details of the numerical solution of (29)–(30) are given in Appendix C. A key test of the accuracy of the numerical solution is to check for consistency with the effective diffusivity results of section 3.2. A property of the Legendre transform pair (31) is that $f'''(0)g''(0) = 1$, from which it follows that $\kappa_{\text{eff}} = f''(0)/2$. From the Maclaurin expansion, using the fact that $f(0) = f'(0) = 0$, it follows that $\kappa_{\text{eff}} = \lim_{q \rightarrow 0} f(q)/q^2$. Consequently a numerical estimate for κ_{eff} can be obtained by solving (29)–(30) for suitably small q . The calculated values of κ_{eff} are plotted in Figure 2 (blue curves) and show excellent agreement with the analytical results (24)–(25) for $\delta \lesssim 1$, as well as the numerical results from the RFM itself. Importantly, these results give confidence in the accuracy of the numerical solver at finite q , and thus the resulting rate function $g(\xi)$ obtained by numerical inversion of (31).

Figures 3(a)–(c) shows $g(\xi)$ calculated for the three profiles in Table A1 for both the RFM (blue curves) and RDM (red curves). The transitions between inner and outer regions at $\xi = u_{\text{min}}, u_{\text{max}}$ are clearly marked, as is the parabolic approximation $g_0(\xi)$ for the RFM (black dashed curves). In both the RFM and RDM, and for all three profiles, $g(\xi)$ increases rapidly compared to its parabolic

approximation $g_0(\xi)$, as the transitions to the outer region are approached. The result is that particle concentrations fall off particularly rapidly compared to the Gaussian approximation. The neutral profile exhibits an interesting asymmetry, in that $g(\xi)$ increases more rapidly for negative ξ than for positive ξ . The explanation is that the vertical diffusivity $\kappa_2(z)$ is rather small towards the top of the domain in the neutral case. Parcels therefore have comparatively long residence times in the upper part of the domain, where the velocity is large and positive, compared to near the ground where the velocity is large and negative. Hence it is more probable that a parcel remains close to $z = 1$ and experiences a large net positive transport than the corresponding negative transport near $z = 0$.

Figures 3(d)–(f) show the percentage difference between the RFM and RDM results, and show that the small differences reported in κ_{eff} are not typical of the differences in $g(\xi)$ everywhere. In both the stable and neutral profiles, in the downstream tail $g(\xi)$ is significantly larger ($\gtrsim 20\%$) for the RDM. It follows that the effect of realistic Lagrangian decorrelation times in the RFM is to enhance transport into the tail regions. The effect is largest in the downstream tail because those trajectories are in the upper part of the domain where the local Lagrangian time-scales are longest.

In fact as $\xi \rightarrow \pm\infty$, the rate functions for the RDM and RFM can be expected to converge, because in this limit the contribution of the mean flow can be neglected completely. In that case the horizontal component of (5) is a canonical Ornstein–Uhlenbeck process, whereas that of (9) is a simple Brownian process, each of which have identical (quadratic) rate functions. There is a strong hint of this convergence at large $|\xi|$ in the ideal and stable calculations shown in Figure 3.

To demonstrate that large-deviation theory correctly captures the spatial structure of the distribution of particles in the tail regions, Figure 4 compares normalized vertical profiles of concentration, according to the theory (28) (curves), and from an ensemble of RFM calculations (3) (points). The stable ABL scenario of Table A1 (also Figure 1) is used, and Figure 4(a) shows results at $t = 20$ at various positions in the positive tail region, with (b) showing the negative tail.

Direct Monte-Carlo simulation of (3) is too expensive, by some orders of magnitude, to obtain the necessary statistics in the tail regions to generate the plots shown in Figure 4. For example, the concentration $\langle c \rangle(x = 45, t = 20) \approx 5 \times 10^{-7}$, indicating that at the end of a direct calculation, only one in every two million trajectories will be located within a unit area surrounding the measurement site. To overcome this problem, the unbiased pruning and cloning method ‘go-with-the-winners’

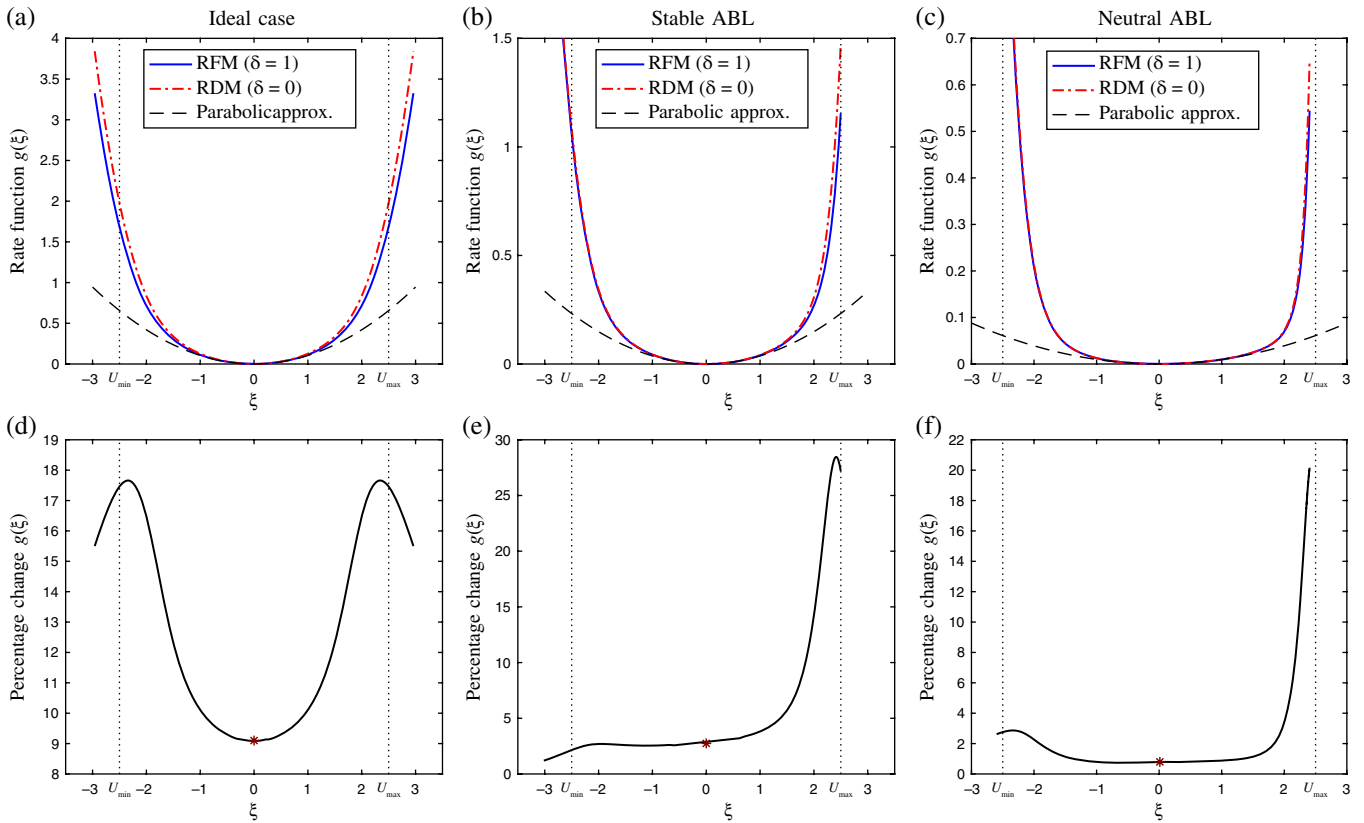


Figure 3. Rate function $g(\xi)$ for the RFM (solid curves, blue online) and RDM (dot-dash curves, red online), and the parabolic approximation $g_0(\xi)$ for the RFM (dashed curves, black online), for (a) the ideal (constant with height), (b) stable ABL and (c) neutral ABL conditions, as detailed in Table A1. (d)–(f) show percentage differences between $g(\xi)$ in the RFM and in the RDM (calculated as $100(\text{RFM} - \text{RDM})/\text{RDM}$). [Colour figure can be viewed at [wileyonlinelibrary.com](#)].

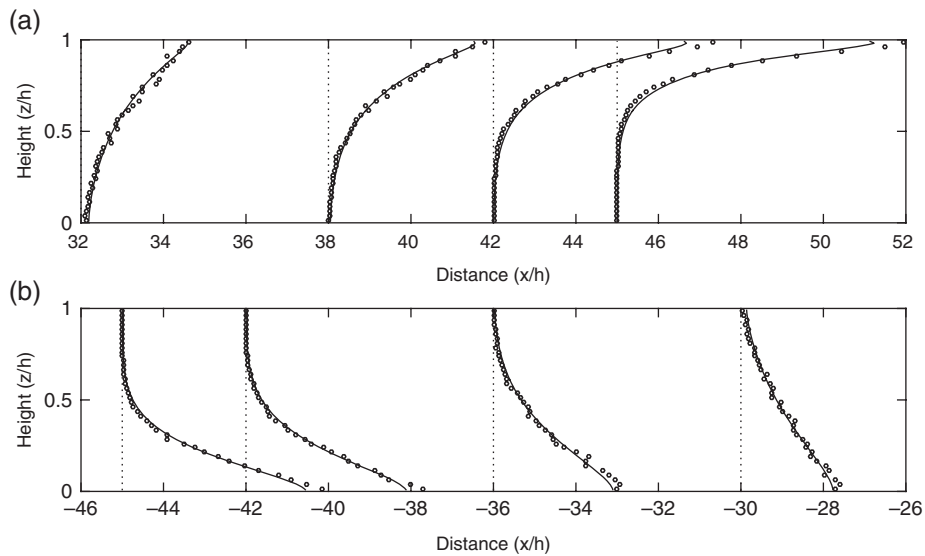


Figure 4. Normalised profiles of concentration $c(x_0, z, t_0)$ at $t_0 = 20$ in the tails of the stable ABL calculation shown in Figure 1. (a) $x_0 = 32, 38, 42$ and 45 , and (b) $x_0 = -30, -36, -42$ and -45 . The curves are the large-deviation approximation, calculated from the eigenfunctions $\phi(z, \omega, \lambda, \xi)$ obtained from (29). The points are obtained directly from Monte-Carlo simulation of (3) augmented by the ‘go-with-the-winners’ algorithm (see text).

(GWTW; Grassberger, 2002) is used to focus the calculation, following Haynes and Vanneste (2014). The key to the successful implementation of GWTW is a suitable choice of scoring function, used to decide which trajectories are to be pruned/cloned. Here, following the argument of Esler (2015), the scoring function is chosen to be the product of each trajectory’s current weight and a local approximation to the solution of the appropriate adjoint problem. The adjoint problem in this case is the ‘reverse-time’ transport problem, solved backwards from the receptor where the measurement is to be taken. For a receptor at (x_0, t_0) in the tail region, with $x_0/t_0 = \xi_0$ (say), the adjoint concentration can be crudely estimated from the large deviation form, which by

symmetry with the forward problem, is

$$c^*(x, z, t) \sim (t_0 - t)^{-1/2} \phi^*(z, \xi^*) e^{-(t_0 - t) g(\xi^*)}, \quad (32)$$

where $\xi^* = (x_0 - x)/(t_0 - t)$, and $g(\cdot)$ is the same rate function as in the forward problem. Expanding $g(\xi^*)$ around ξ_0 , the leading-order x -dependence is given by

$$c^* \approx e^{q_0(x-x_0)}, \quad q_0 = g'(\xi_0). \quad (33)$$

Choosing the scoring function based on (33) consequently acts to focus trajectories in the GWTW calculation along the ‘ray’

$x/t = \xi_0$, with ξ_0 being related to q_0 through the Legendre transform (31). The result is that, by the end of the calculation, a large number of trajectories end up close to the receptor region ($x_0 \approx \xi_0 t_0$), with each trajectory weight being suitably adjusted so as to keep the calculation unbiased.

The GWTW Monte-Carlo results shown in Figure 4 are obtained from separate calculations, which differ in the value of q_0 chosen, in order to target each receptor region ($x = 32, 38, 42, 45$, etc.) in turn. It is found that $N = 10^5$ trajectories are required to obtain the agreement shown with the large-deviation predictions. It is notable that there is an asymmetry in the positive and negative tails, which can be explained by the vertical diffusivity being somewhat higher in the lower part of the stable ABL, resulting in an eigenfunction with a thicker boundary layer than in the corresponding position in the forward tail.

3.4. RFM non-uniqueness

It is well-known that the ‘well-mixed’ condition of Thomson (1987) is not sufficient to determine a unique RFM in two or more dimensions. It is interesting to explore how this non-uniqueness can result in changes to κ_{eff} . Arguably the simplest family of non-unique models is obtained by replacing (5) with

$$\left. \begin{aligned} d\Lambda &= -\left(\frac{\Lambda}{\tau_1} + \frac{\Omega}{\tau_r}\right) dt + \left(\frac{2}{\tau_1}\right)^{1/2} dB_1, \\ d\Omega &= \left(-\frac{\Omega}{\tau_2} + \frac{\Lambda}{\tau_r} + \frac{d\sigma_2}{dz}\right) dt + \left(\frac{2}{\tau_2}\right)^{1/2} dB_2, \\ dX &= (u + \Lambda\sigma_1) dt, \\ dZ &= \Omega\sigma_2 dt. \end{aligned} \right\} \quad (34)$$

Here $\tau_r(z)$ can be any smooth function. Its (local) interpretation is that $|\tau_r|$ is a ‘rotational’ time-scale which controls the rate of spin of trajectories in the (x, z) -plane, with the sign of τ_r determining the sense of rotation. The RFM (34) also has the invariant measure (8) and therefore cannot be objectively distinguished from (5).

Since it has been established above that, for late-time dispersion, in practice the RFM model represents only a small correction to the RDM, we will focus only on the latter here. In Appendix B3 the method of homogenization (e.g. Pavliotis and Stuart, 2007) is applied to the RFM to show that, in the RDM limit, the Fokker–Planck equation of (34) is the advection–diffusion equation

$$c_t + \{u + (\kappa_r \Pi)_z\} c_x = \kappa_1 \Pi c_{xx} + (\kappa_2 \Pi c_z)_z. \quad (35)$$

Here $\kappa_i = \sigma_i^2 \tau_i$ for $i = 1, 2$ as above, $\kappa_r = \sigma_1 \sigma_2 \tau_1 \tau_2 / \tau_r$ and

$$\Pi = \frac{\tau_r^2}{\tau_r^2 + \tau_1 \tau_2} \quad (36)$$

is a non-dimensional ‘diffusivity suppression factor’ which takes values in the range $0 < \Pi \leq 1$. Notice that in the limit $\tau_r \rightarrow \pm\infty$, in which (34) \rightarrow (5), $\Pi \rightarrow 1$ and $\kappa_r \rightarrow 0$, so that (35) reduces to (10).

The consequence of using the general RFM (34) in place of (5) is therefore generally to increase the effective horizontal diffusivity by reducing the physical vertical diffusivity. The effective diffusivity result analogous to that in (2) is

$$\kappa_{\text{eff}} = \left\langle \frac{\bar{F}^2}{\kappa_2 \Pi} + \kappa_1 \Pi \right\rangle, \quad (37)$$

where $\bar{F}(z)$ is modified from $F(z)$,

$$\bar{F}(z) = F(z) + \kappa_r(z)\Pi(z) - \kappa_r(0)\Pi(0). \quad (38)$$

Note that the mean advecting velocity in (2) is also modified to $\{u + (\kappa_r \Pi)_z\}$.

3.5. Three-dimensional effects

Three-dimensional dispersion in the ABL merits separate consideration in order to understand the effect of the turning of the mean wind with height, i.e. in Ekman layers. Assuming horizontally isotropic statistics, the three-dimensional extension of the RDM (9) has Fokker–Planck equation

$$c_t + \mathbf{u} \cdot \nabla_H c = \kappa_H \nabla_H^2 c + (\kappa_V c_z)_z, \quad (39)$$

where $\mathbf{u}(z) = \{u_1(z), u_2(z)\}^T$ is the (2D) horizontal mean wind profile, ∇_H denotes the horizontal gradient operator and $\kappa_H = \sigma_1^2 \tau_1$ and $\kappa_V = \sigma_2^2 \tau_2$, as obtained from the profiles in Table A1.

Applying the homogenisation procedure to the RDM (39), in order to obtain its long-time behaviour, results in the two-dimensional analogue of (2)

$$\partial_t \langle c \rangle + \langle \mathbf{u} \rangle \cdot \nabla_H \langle c \rangle = \nabla_H \cdot (\kappa_{\text{eff}} \cdot \nabla_H \langle c \rangle). \quad (40)$$

Here the effective diffusivity tensor κ_{eff} , split into a shear dispersion term $\kappa_{\text{eff}}^{(1)}$ and a direct dispersion term $\kappa_{\text{eff}}^{(2)}$, is given by

$$\kappa_{\text{eff}}^{(1)} = \begin{pmatrix} \langle F_1^2 / \kappa_V \rangle & \langle F_1 F_2 / \kappa_V \rangle \\ \langle F_1 F_2 / \kappa_V \rangle & \langle F_2^2 / \kappa_V \rangle \end{pmatrix}, \quad (41)$$

where

$$F_i(z) = \int_0^z \{u_i(\bar{z}) - \langle u_i \rangle\} d\bar{z}, \quad (42)$$

and $\kappa_{\text{eff}}^{(2)} = \kappa_{\text{eff}}^{(2)} \mathbf{I}$, where $\kappa_{\text{eff}}^{(2)} = \langle \kappa_H \rangle$ and \mathbf{I} is the identity matrix.

In typical ABL conditions the tensor $\kappa_{\text{eff}}^{(1)}$ can be expected to be strongly anisotropic. It has eigenvalues

$$\kappa_{\text{eff}}^{\pm} = \left\langle \frac{F^2}{2\kappa_V} \right\rangle \{1 \pm (1 - \Gamma)^{1/2}\}, \quad (43)$$

where $F = (F_1^2 + F_2^2)^{1/2}$ and Γ is a measure of anisotropy, taking values in the range $0 \leq \Gamma \leq 1$, given by

$$\Gamma = 4 \frac{\langle F_1^2 / \kappa_V \rangle \langle F_2^2 / \kappa_V \rangle - \langle F_1 F_2 / \kappa_V \rangle^2}{\langle F^2 / \kappa_V \rangle^2}. \quad (44)$$

Notice that Γ is invariant under a coordinate rotation about the vertical axis.

The eigenvalues give the effective diffusion rate in the principal directions given by the associated eigenvectors (approximately, the major axis associated with κ_{eff}^+ is in the direction of $\langle F \kappa_V^{-1/2} \rangle$ where $\mathbf{F} = (F_1, F_2)^T$, and the minor axis associated with κ_{eff}^- is perpendicular to this). When there is no turning of the wind with height, then $\Gamma = 0$ and $\kappa_{\text{eff}}^- = 0$, meaning that shear dispersion acts in one direction only.

The physics of the three-dimensional ABL dispersion changes significantly based on the ordering of the diffusivities κ_{eff}^+ , $\kappa_{\text{eff}}^{(2)}$ and κ_{eff}^- . Generally, $\mathcal{U} \gtrsim 1$ and $\kappa_{\text{eff}}^+ \gg \kappa_{\text{eff}}^-, \kappa_{\text{eff}}^{(2)}$, so the interesting question concerns the relative magnitudes of κ_{eff}^- and $\kappa_{\text{eff}}^{(2)}$. The answer is important, as the effective diffusivity along the minor axis will control the width of emission plumes far downstream of sources, and consequently their rate of mixing into the environment. The two regimes are:

- 2D shear dispersion (2D-SD) regime ($\kappa_{\text{eff}}^- > \kappa_{\text{eff}}^{(2)}$). In this regime shear dispersion dominates along the minor axis, and the plume width will be proportional to the magnitude of the wind strength, and inversely proportional to the square root of the vertical diffusivity.

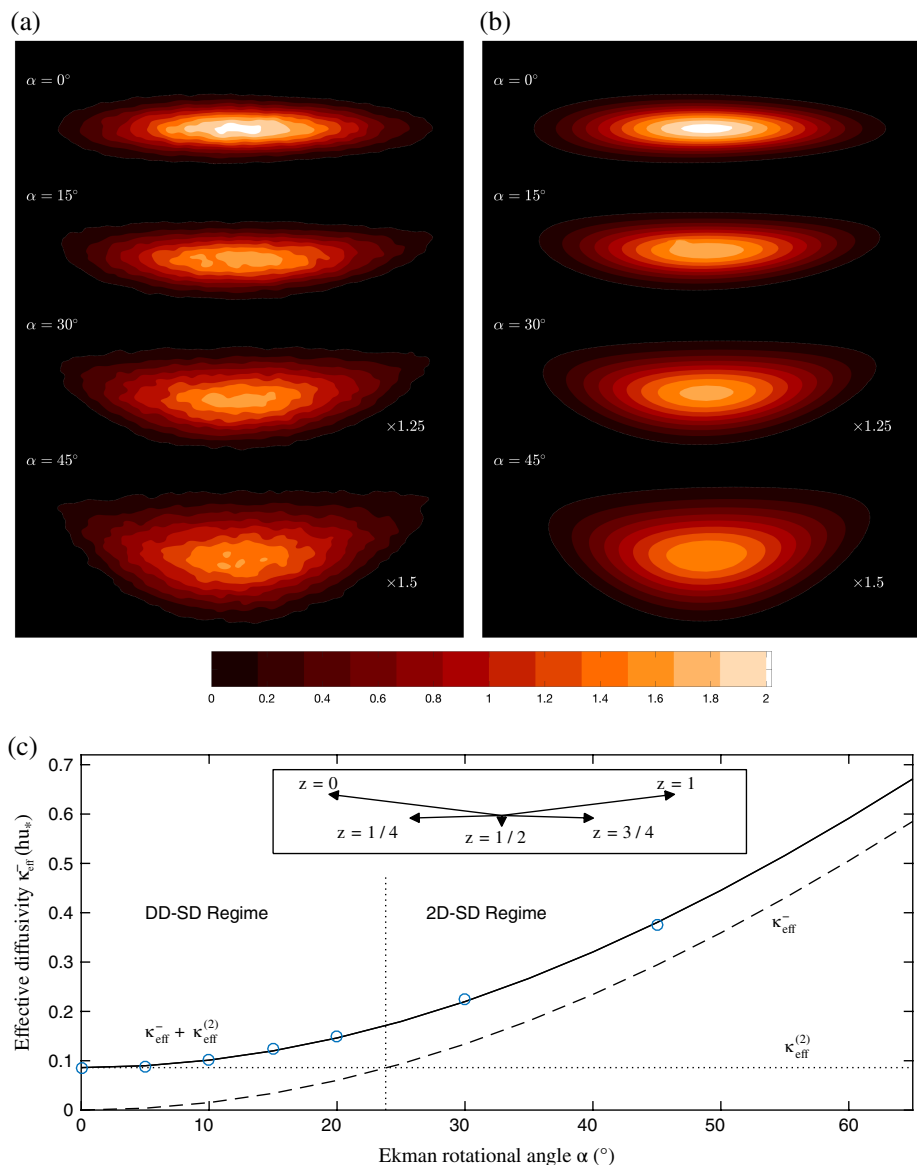


Figure 5. (a) Contour plots of vertically integrated particle concentration density $\langle c \rangle(x, y, t)$ at $t = 30hu_*^{-1}$, in RDM experiments with $N = 10^5$ trajectories. The mean ABL velocity is the Ekman spiral flow (45), with parameters $\mathcal{U} = 10$ and $\alpha = 0^\circ, 15^\circ, 30^\circ$ and 45° (top to bottom), and with κ_H and κ_V corresponding to stable ABL conditions. For clarity, the concentration fields have been rotated so that the major axis is parallel to the x -axis, and the box dimensions are 200×100 (this aspect ratio is chosen in order to show detail in the y -direction). Concentration units are $10^{-4}h^{-2}$ with the total amount of tracer fixed at unity. (b) Concentration fields for the same conditions calculated from the large-deviation approximation (48). (c) Total effective diffusivity $\kappa_{\text{eff}}^- + \kappa_{\text{eff}}^{(2)}$ in the minor axis direction as a function of α . The solid line is the theory (43) and the points are calculated from integrations of the RDM. The dotted line shows $\kappa_{\text{eff}}^{(2)}$ and the dashed curve κ_{eff}^- , with their intersection at α_c . The inset shows the relative velocity $\mathbf{u} - \langle \mathbf{u} \rangle$ in the Ekman spiral, rotated so that the mean shear is in the x -direction. [Colour figure can be viewed at wileyonlinelibrary.com].

- Direct dispersion-shear diffusion (DD-SD) regime ($\kappa_{\text{eff}}^{(2)} > \kappa_{\text{eff}}^-$). In contrast, in the DD-SD regime plume widths will be sensitive only to the vertical mean of the direct horizontal diffusivity κ_H .

The diffusivities $\kappa_{\text{eff}}^+, \kappa_{\text{eff}}^{(2)}$ and κ_{eff}^- can be evaluated for the profiles of turbulent statistics given in Table A1. Taking a linear shear flow with an Ekman spiral

$$\mathbf{u} = \mathcal{U}z \{ \cos(\alpha z), \sin(\alpha z) \}^T, \quad (45)$$

and using the fact that in the ideal profile $\kappa_V = \kappa_H = \kappa$, the integrals in (43) can be evaluated exactly. The leading order result for $\alpha \ll 1$ is the most illuminating,

$$\kappa_{\text{eff}}^+ = \frac{\mathcal{U}^2}{120\kappa}, \quad \kappa_{\text{eff}}^- = \frac{\mathcal{U}^2}{120\kappa} \frac{\alpha^2}{63}. \quad (46)$$

The result for κ_{eff}^+ is well-known as the one-dimensional effective diffusivity for a linear shear flow with a constant diffusivity

(e.g. Saffman 1962, their Eq. 17). The formula for κ_{eff}^- is striking, because it shows that for $\alpha \lesssim 1$ (radians) the effective diffusivity in the direction of the minor axis will be weaker by two to three orders of magnitude or more. (The small-angle approximation (46) is useful throughout this range, as the error relative to the exact result (43) is just 7% for $\alpha = 1$ radian). The result (46) allows the critical angle α_c , defined to be the angle α for which $\kappa_{\text{eff}}^- = \kappa_{\text{eff}}^{(2)}$, to be estimated. It follows that ABLs with $\alpha \lesssim \alpha_c$ are in the DD-SD regime and those with $\alpha \gtrsim \alpha_c$ in the 2D-SD regime described above. Inserting $\kappa_{\text{eff}}^{(2)} = \kappa = 0.1$ for the ideal profile gives (in radians)

$$\alpha_c = D\mathcal{U}^{-1}, \quad \text{with } D = \left(\frac{7560}{100} \right)^{1/2} \approx 8.69. \quad (47)$$

Similar calculations can be made numerically for the stable and neutral profiles, for which (47) also applies, but with $D \approx 4.16$ and $D \approx 0.793$ respectively. The lower value of D in the neutral case results in smaller values of α_c , meaning that, compared to

the stable case, a wider region of (\mathcal{U}, α) parameter space is in the 2D-SD regime than in the DD-SD regime.

Figure 5(a) shows $\langle c \rangle(x, y, t)$ at $t = 30hu_*^{-1}$ from three-dimensional RDM calculations in the stable ABL with $\mathcal{U} = 10$ and $\alpha = 0^\circ, 15^\circ, 30^\circ$ and 45° . Trajectories are released at $(0, 0, 1/2)$ in each case. Based on (47) $\alpha_c \approx 24^\circ$. The $\alpha = 0^\circ$ and 15° calculations are well within the DD-SD regime, and show near-identical diffusion rates in the direction of the minor (y) axis. The third and fourth calculations with $\alpha = 30^\circ$ and 45° are in the 2D-SD regime and have a clearly increased rate of diffusion in the minor axis direction.

Figure 5(c) shows the total effective diffusivity in the minor axis direction $\kappa_{\text{eff}}^- + \kappa_{\text{eff}}^{(2)}$ as a function of α . Estimates from the RDM integrations results are shown as solid points, and the solid curve shows the theoretical prediction (43), which is seen to be accurate in this parameter regime. The transition between the DD-SD and 2D-SD regimes occurs at $\alpha_c \approx 24^\circ$.

It is notable that the plumes in Figure 5 begin to bend once $\alpha \gtrsim \alpha_c$. A similar bending of pollutant plumes has been reported in large-eddy simulations (LESs) in stable ABL conditions by Kemp and Thomson (1996), who attribute the phenomenon (as here) to the turning of the mean wind with height. The phenomenon is qualitatively easy to understand with reference to the relative wind vectors shown in Figure 5 (inset). Particles making large excursions along the major axis spend more time near the top or bottom of the ABL, where they experience a positive relative flow in the minor axis (here y) direction, whereas particles staying near the domain centre tend to sample a negative relative flow.

The large-deviation framework introduced in section 2.2 allows the bending of the plume to be quantified, by seeking a solution of (39) of the form

$$c(x, y, z, t) \sim t^{-1} \phi(z, \xi) e^{-t g(\xi)}, \quad \xi = (x, y)^T / t. \quad (48)$$

The eigenvalue problem satisfied by ϕ is found to be (cf. Haynes and Vanneste, 2014)

$$(\kappa_V \phi_z)_z + (\mathbf{u} \cdot \mathbf{q} + \kappa_H |\mathbf{q}|^2) \phi = f(\mathbf{q}) \phi, \quad (49)$$

$$\phi_z = 0, \quad z = 0, 1.$$

where $\mathbf{q} = \nabla_{\xi} g$. The rate function $g(\xi)$ is related to the eigenvalues $f(\mathbf{q})$ via the Legendre transform

$$g(\xi) = \sup_{\mathbf{q}} \{ \xi \cdot \mathbf{q} - f(\mathbf{q}) \}. \quad (50)$$

To obtain $g(\xi)$ numerically, it is necessary to solve (49) numerically for \mathbf{q} taking values over a regular grid, recording the principal eigenvalue $f(\mathbf{q})$ everywhere on the grid. A standard nonlinear programming algorithm (with cubic interpolation) can then be used to solve (50). Figure 5(b) shows the prediction (48), using the calculated $g(\xi)$. A caveat is that the approximation used is somewhat crude, because for simplicity we have made the (unjustified) assumption that $\langle \phi \rangle$ is independent of ξ . However, notwithstanding this caveat, it is clear that the large-deviation theory does a good job of capturing the extent of the plume bending effect accurately over this time interval.

4. Conclusions

The main results of this study can be summarized as follows:

1. Horizontal effective diffusivity κ_{eff} in the ABL, under realistic stable or neutral conditions, differs by at most a few percent depending on whether particle dispersion is modelled by the RFM or its RDM approximation. The analytical formulae (24)–(25) allow the RFM \rightarrow RDM correction to κ_{eff} to be calculated for arbitrary vertical profiles of velocity and turbulent statistics. The insensitivity

of κ_{eff} supports the choice of researchers using models based on the RDM (e.g. the model MLPD0; D'Amours *et al.*, 2010) for applications involving large-scale dispersion. In fact, given that existing RFM 'long' time-stepping schemes (e.g. Legg and Raupach, 1982) introduce large numerical errors at operational time steps (Ramli and Esler, 2016), it is reasonable to conclude that, given finite computational resources, the RDM will be more accurate and robust for a wide class of dispersion problems for which the RFM is often currently used.

2. The large-deviation rate function ($g(\xi)$ above), which controls the evolution of the tracer concentration in the tail regions of the cloud of particles, is more sensitive to the use of the RDM approximation (Figure 3). In particular, the RFM exhibits increased transport (reduced rate function $g(\xi)$) to the positive tail region for the stable and neutral profiles, compared to the RDM. For transport problems in which the quantity of interest is the first time a concentration meets a given (low) threshold (e.g. the poison release problem), it may be advisable to use the RFM to obtain accurate results.
3. The non-uniqueness of the 'well-mixed' RFM in two dimensions (Thomson, 1987) means that RFMs exist with significantly different κ_{eff} . For example, a rotational component to the trajectory evolution equations can be introduced ((34)). Models with a short rotational time-scale τ_r have significantly suppressed (physical) diffusivity, with a corresponding increase in κ_{eff} .
4. In three-dimensional ABL flows with an Ekman spiral, the effective diffusivity due to shear dispersion in the 'minor axis' direction κ_{eff}^- (approximately perpendicular to the wind shear direction), is typically two orders of magnitude weaker than that along the major axis κ_{eff}^+ , even for wind rotations α of up to a radian. The nature of the resulting ABL dispersion is controlled by the relative magnitudes of κ_{eff}^- and the direct horizontal diffusivity $\langle \kappa_H \rangle$. For $\kappa_{\text{eff}}^- \lesssim \langle \kappa_H \rangle$ (the DD-SD regime above), plume widths are controlled by the direct horizontal diffusivity and straight plumes emerge. For $\kappa_{\text{eff}}^- \gtrsim \langle \kappa_H \rangle$ (the 2D-SD regime above), bent plumes, as observed in LESs of stable conditions (Kemp and Thomson, 1996), are evident. The effective diffusivity reveals no information about plume bending, however its extent can be quantitatively predicted using large-deviation theory.

Acknowledgements

HMR acknowledges support from UBD Chancellor's Scholarship and UCL Studentship.

Appendices

Appendix A: Empirical profiles of turbulent statistics

Throughout the article, three example profiles for $\sigma_i(z)$, the standard deviation of the turbulent velocity field, and $\tau_i(z)$, the corresponding Lagrangian decorrelation time-scales, are used. Here the subscripts $i = 1, 2$ correspond to the x and z -directions respectively. The profiles are detailed in Table A1 (Ramli and Esler, 2016, also give further discussion, including plots (their Figure 1). Briefly, the first is an 'ideal' profile with constant $\sigma_i(z)$ and $\tau_i(z)$ ($i = 1, 2$), which allows for explicit analytical progress. The remaining two profiles are widely used (Hanna, 1982; Stohl *et al.*, 2005) empirical fits to observed statistics in stable and neutral conditions respectively. In practice, the exact profiles suggested by Hanna (1982) are modified slightly (Table A1 caption), to avoid singular behaviour at the ABL top and bottom. This is necessary because in Hanna's original profiles either $\sigma_w \rightarrow 0$ or $\tau \rightarrow 0$ as $z \rightarrow 0, 1$, with neither type of behaviour being physical.

Table A1. Non-dimensional profiles of the velocity standard deviation $\sigma_i(z)$ ($i = 1, 2$) and Lagrangian decorrelation time-scale $\tau_i(z)$ for three possible ABL situations: (i) ideal (constant) profile, (ii) stable ABL, and (iii) neutral ABL 3 (e.g. Hanna, 1982).

	$\sigma_1(z)$ $\sigma_2(z)$	$\tau_1(z)$ $\tau_2(z)$
Ideal	1 1	0.1 0.1
Stable	$2.0(1-z)$ $1.3(1-z)$	$0.15z^{1/2}/\sigma_1$ $0.1z^{4/5}/\sigma_2$
Neutral	$2.0 \exp(-2z/\epsilon)$ $1.3 \exp(-2z/\epsilon)$	$\frac{2\sigma_2(1+15z/\epsilon)}{z}$ $\frac{2\sigma_2(1+15z/\epsilon)}{z}$

The units are u_* and hu_*^{-1} respectively. The parameter $\epsilon = u_* / fh$ in the neutral profile is set to 0.8. In the case of the stable and neutral profiles, regularized profiles ($\bar{\sigma}_i(z), \bar{\tau}_i(z)$) are used in practice, where $\bar{\sigma}_i(z) = \sigma_i(Z_m(z))$ and $Z_m(z) = z_b + z(1 - 2z_b)$ for $z_b = 0.05$.

Appendix B: Mathematical details

B1. Properties of (probabilists') Hermite polynomials

In this appendix we detail some useful properties of the probabilists' Hermite polynomials. The k th polynomial, denoted $He_k(\omega)$, is defined by

$$He_k(\omega) = (-1)^k e^{\omega^2/2} \frac{d^k}{d\omega^k} e^{-\omega^2/2}. \tag{B1}$$

Associated with each polynomial is a Hermite function $He_k(\omega)e^{-\omega^2/2}/\sqrt{2\pi}$. Here we give those identities used in the derivation of (B8), (B11) and (C2). All are standard results (e.g. Abramowitz and Stegun, 1965, chapter 22).

First, the Hermite polynomials are solutions of Hermite's equation

$$\left(\frac{\partial^2}{\partial \omega^2} - \omega \frac{\partial}{\partial \omega}\right) He_k(\omega) = -k He_k(\omega), \tag{B2}$$

from which it follows that the Hermite functions satisfy

$$\left(\frac{\partial^2}{\partial \omega^2} + \omega \frac{\partial}{\partial \omega} + 1\right) \left(\frac{He_k(\omega)e^{-\omega^2/2}}{\sqrt{2\pi}}\right) = -k \frac{He_k(\omega)e^{-\omega^2/2}}{\sqrt{2\pi}}. \tag{B3}$$

Second, because Hermite's equation can be written as an eigenvalue problem with a self-adjoint linear operator, the Hermite polynomials can be shown to satisfy an orthogonality relation, specifically

$$\int_{-\infty}^{\infty} He_j(\omega) He_k(\omega) \frac{e^{-\omega^2/2}}{\sqrt{2\pi}} d\omega = k! \delta_{jk}, \tag{B4}$$

where δ_{jk} is the Kronecker delta. Notice that a special case of (B4), for $j = 0$, is the integral identity

$$\int_{-\infty}^{\infty} He_k(\omega) e^{-\omega^2/2} d\omega = 0, \quad (k \geq 1). \tag{B5}$$

Thirdly and fourthly, the following differentiation and recursion relations can be obtained:

$$\frac{d}{d\omega} He_k(\omega) = k He_{k-1}(\omega), \tag{B6}$$

$$\omega He_k(\omega) = He_{k+1}(\omega) + k He_{k-1}(\omega). \tag{B7}$$

The results (B3)–(B7) are essential to the derivation of the systems of Eqs (B8), (B11) and (C2).

B2. Asymptotic solution for p_1 in Eq. (18)

To find the effective diffusivity in the calculation of section 3.1 the particular integral for (18) must be found. The details follow. First note that the boundary conditions require $C_k(0) = C_k(1) = 0$ and $D_k(0) = D_k(1) = 0$ for k odd.

Inserting the expansion (19) into (18), the following hierarchy is obtained for the $\{C_k\}$,

$$\left. \begin{aligned} 0 &= \delta(\bar{\sigma}_2 C_1)' + \delta^2 u & k = 0, \\ -\frac{kC_k}{\bar{\tau}_2} &= \delta \bar{\sigma}_2 C_{k-1}' + \delta(k+1)(\bar{\sigma}_2 C_{k+1})' & k \geq 1. \end{aligned} \right\} \tag{B8}$$

The first equation can be integrated to obtain

$$C_1(z) = -\delta \bar{\sigma}_2^{-1} F(z). \tag{B9}$$

Notice that the boundary conditions are satisfied because $F(0) = F(1) = 0$. Rearranging the $k = 1$ equation,

$$\begin{aligned} C_0' &= \frac{F}{\kappa_2} - 2 \frac{(\bar{\sigma}_2 C_2)'}{\bar{\sigma}_2} \\ &= \frac{F}{\kappa_2} - \frac{\delta^2}{\bar{\sigma}_2} \left\{ \kappa_2 \left(\frac{F}{\bar{\sigma}_2} \right)' \right\}' + \frac{3\delta (\bar{\sigma}_2 \bar{\tau}_2 (\bar{\sigma}_2 C_3)')'}{\bar{\sigma}_2}, \end{aligned} \tag{B10}$$

where the $k = 2$ equation of (B8) has been used to substitute for C_2 .

Inserting the above expression for C_0' into (23) for $\kappa_{\text{eff}}^{(1)}$, integrating by parts, and using the fact that $C_3(0) = C_3(1) = 0$, gives

$$\kappa_{\text{eff}}^{(1)} = \left\langle \frac{F^2}{\kappa_2} + \delta^2 \kappa_2 \left(\frac{F}{\bar{\sigma}_2} \right)'^2 + 3\delta C_3 \bar{\sigma}_2 \left\{ \frac{\kappa_2}{\bar{\sigma}_2} \left(\frac{F}{\bar{\sigma}_2} \right)' \right\}' \right\rangle.$$

Using the $k = 3$ equation of (B8) to substitute for C_3 , and integrating by parts again, results in (after some working)

$$\begin{aligned} \kappa_{\text{eff}}^{(1)} &= \left\langle \frac{F^2}{\kappa_2} + \delta^2 \kappa_2 \left(\frac{F}{\bar{\sigma}_2} \right)'^2 - \frac{\delta^4}{2} \kappa_2 \left\{ \frac{\kappa_2}{\bar{\sigma}_2} \left(\frac{F}{\bar{\sigma}_2} \right)' \right\}'^2 \right\rangle \\ &\quad + O(\delta^6), \end{aligned}$$

from which the result (24) follows upon substitution of $\delta\sigma_2$ for $\bar{\sigma}_2$.

The explicit horizontal diffusivity $\kappa_{\text{eff}}^{(2)}$ can be handled in a similar fashion. The corresponding hierarchy is

$$\left. \begin{aligned} -\frac{D_0}{\bar{\tau}_1} &= \delta(\bar{\sigma}_2 D_1)' + \delta \bar{\sigma}_1 & \text{for } k = 0, \\ -\frac{\bar{\tau}_2 + k\bar{\tau}_1}{\bar{\tau}_1 \bar{\tau}_2} D_k &= \delta \bar{\sigma}_2 D_{k-1}' + \delta(k+1)(\bar{\sigma}_2 D_{k+1})' & \text{for } k \geq 1. \end{aligned} \right\} \tag{B11}$$

Following the same procedure as above

$$\begin{aligned} \kappa_{\text{eff}}^{(2)} &= -\delta^{-1} \langle \bar{\sigma}_1 D_0 \rangle \\ &= \langle \bar{\sigma}_1^2 \bar{\tau}_1 + \bar{\sigma}_2 D_1 (\bar{\sigma}_1 \bar{\tau}_1)' \rangle, \end{aligned}$$

where the second expression is obtained by substituting for D_0 from (B11) and integrating by parts. It follows from the $k = 1$ equation of (B11) that

$$\bar{\sigma}_2 D_1 = \delta^2 \frac{\bar{\tau}_1 \bar{\tau}_2}{\bar{\tau}_1 + \bar{\tau}_2} \bar{\sigma}_2^2 (\bar{\sigma}_1 \bar{\tau}_1)' + O(\delta^4),$$

from which

$$\kappa_{\text{eff}}^{(2)} = \left\langle \kappa_1 + \delta^2 \frac{\kappa_2 \bar{\tau}_1}{\bar{\tau}_1 + \bar{\tau}_2} \left(\frac{\kappa_1}{\bar{\sigma}_1} \right)'^2 \right\rangle + O(\delta^4).$$

The result (25) follows upon substitution of $\delta\sigma_i$ for $\bar{\sigma}_i$ and $\delta^{-2}\tau_i$ for $\bar{\tau}_i$ ($i = 1, 2$).

B3. The RDM limit of the generalized RFM (34)

Here, the RDM limit of the generalized ‘non-unique’ RFM (34) is obtained, using the method of homogenization (e.g. Pavliotis and Stuart, 2008). The starting point is the Fokker–Planck equation of (34), which following the substitution (13) is

$$\delta^2 p_t + \{(\delta^2 u + \delta \lambda \bar{\sigma}_1) p\}_x + \delta (\omega \bar{\sigma}_2 p)_z + \delta (\bar{\sigma}'_2 p)_\omega = \mathcal{L}_r p, \quad (\text{B12})$$

where the linear operator \mathcal{L}_r acts on functions $f(\lambda, \omega, z)$ according to

$$\begin{aligned} \mathcal{L}_r f \equiv & \bar{\tau}_1^{-1} (f_\lambda + \lambda f)_\lambda + \bar{\tau}_2^{-1} (f_\omega + \omega f)_\omega \\ & + \bar{\tau}_r^{-1} (\omega f_\lambda - \lambda f_\omega). \end{aligned} \quad (\text{B13})$$

The Fokker–Planck of the RDM is recovered in the limit $\delta \ll 1$. Expanding p as a power series in δ ,

$$p = p_0 + \delta p_1 + \dots, \quad (\text{B14})$$

the leading-order equation is found to be $\mathcal{L}_r p_0 = 0$ which has the ‘well-mixed in velocity-space’ solution

$$p_0 = c(x, z, t) \exp\left\{-\frac{1}{2}(\lambda^2 + \omega^2)\right\}, \quad (\text{B15})$$

where c is at this stage an undetermined concentration field. At next order

$$\begin{aligned} \mathcal{L}_r p_1 = & \lambda \bar{\sigma}_1 p_{0x} + (\omega \bar{\sigma}_2 p_0)_z + (\bar{\sigma}'_2 p_0)_\omega \\ = & (\lambda \bar{\sigma}_1 c_x + \omega \bar{\sigma}_2 c_z) \exp\left\{-\frac{1}{2}(\lambda^2 + \omega^2)\right\}, \end{aligned} \quad (\text{B16})$$

which has the particular integral

$$\begin{aligned} p_1 = & \left\{ -\lambda \bar{\tau}_1 \left(\bar{\sigma}_1 c_x + \frac{\bar{\tau}_2}{\bar{\tau}_r} \bar{\sigma}_2 c_z \right) - \omega \bar{\tau}_2 \left(-\frac{\bar{\tau}_1}{\bar{\tau}_r} \bar{\sigma}_1 c_x + \bar{\sigma}_2 c_z \right) \right\} \\ & \times \left(1 + \frac{\bar{\tau}_1 \bar{\tau}_2}{\bar{\tau}_r^2} \right)^{-1} \exp\left\{-\frac{1}{2}(\lambda^2 + \omega^2)\right\}. \end{aligned} \quad (\text{B17})$$

At $O(\delta^2)$,

$$\mathcal{L}_r p_2 = p_{0t} + u p_{0x} + \lambda \bar{\sigma}_1 p_{1x} + (\omega \bar{\sigma}_2 p_1)_z + (\bar{\sigma}'_2 p_1)_\omega. \quad (\text{B18})$$

The solvability condition for this equation is that the integral over $(\lambda, \omega) \in \mathbb{R}^2$ of the right-hand side must be identically zero. Inserting for p_0 and p_1 and evaluating this integral leads directly to (35).

Appendix C: Solution of the eigenvalue problem (29)–(30)

The numerical method used for the solution of the eigenvalue problem (29)–(30) is as follows. First, ϕ is expanded

$$\begin{aligned} \phi(z, \lambda, \omega, \xi) = & \frac{1}{2\pi} \sum_{k=0}^{\infty} \sum_{l=0}^{\infty} C_{k,l}(z, \xi) \\ & \times \text{He}_k(\omega) \text{He}_l(\lambda) e^{-(\lambda^2 + \omega^2)/2}, \end{aligned} \quad (\text{C1})$$

in the Hermite polynomials $\text{He}_k(\cdot)$ detailed in Appendix B1. The expansion (C1) is then inserted into (29). Using the Hermite polynomial identities given in Appendix B1, the resulting expression can be rearranged into a single summation of the same form as (C1). Using orthogonality, the system can be then be reduced to a doubly-infinite set of coupled ordinary differential equations for the $\{C_{k,l}\}$,

$$\begin{aligned} u q C_{k,l} + \sigma_1 q \{ & C_{k,l-1} + (l+1) C_{k,l+1} \} \\ & - \sigma_2 \partial_z C_{k-1,l} - (k+1) \partial_z (\sigma_2 C_{k+1,l}) \\ & - (k \tau_2^{-1} + l \tau_1^{-1}) C_{k,l} = f(q) C_{k,l}, \end{aligned} \quad (\text{C2})$$

where $k, l \geq 0$, and the convention $C_{k,-1} \equiv 0$ and $C_{-1,l} \equiv 0$ is used. The boundary conditions at $z = 0, 1$ are

$$C_{k,l}(0) = C_{k,l}(1) = 0, \quad \text{for } k \text{ odd}, \quad (\text{C3})$$

and there are no boundary conditions for k even.

The system (C2) can be truncated at finite $(k, l) = (K, L)$, and discretized using M points in z , resulting in a matrix eigenvalue problem of the form

$$\mathbf{A} \mathbf{c} = f(q) \mathbf{c}, \quad (\text{C4})$$

where the square matrix \mathbf{A} has dimension $(K+1)(L+1)M \times (K+1)(L+1)M$. The vector \mathbf{c} has components $\{C_{k,l}(z_m); k=0, \dots, K; l=0, \dots, L; m=1, \dots, M\}$. The vertical discretization, based on the grid $\{z_m = (m - \frac{1}{2})/M; m=1, \dots, M\}$, is discussed in detail in Appendix A of Ramli and Esler (2016) as there are some subtleties related to the implementation of the boundary conditions. In particular, the system will have the correct number of boundary conditions only in the event that the series is truncated at $k = K$ odd. The discretised eigenvalue problem (C4) is solved using the QR-algorithm adapted for sparse matrices, as implemented in the MATLAB routine ‘eigs’ (Lehoucq *et al.*, 1998).

To accelerate the calculations, a multi-grid approach is used. Low-resolution solutions are first used to identify the principal eigenmode. The low-resolution calculations are then interpolated and used as initial guesses for higher-resolution calculations in which only the principal eigenmode is sought. A continuation method is used where calculations at new values of q are initialized with solutions at nearby values. For the profiles detailed in Table A1, the Hermite polynomial expansion converges sufficiently rapidly that errors below the truncation error are obtained for $(K, L) = (7, 5)$. The highest vertical resolution used is $M = 100$. Further details, including an analysis of numerical convergence, are given in Ramli (2016).

References

- Abramowitz M, Stegun I. 1965. *Handbook of Mathematical Functions*. Dover Publications: Mineola, NY.
- Aris R. 1956. On the dispersion of a solute in a fluid flowing through a tube. *Proc. R. Soc. London A*. **235**: 67–77.
- Camassa R, Lin Z, McLaughlin RM. 2010. The exact solution of the scalar variance in pipe and channel flow. *Commun. Math. Sci.* **8**: 601–626.
- Esler JG. 2015. Adaptive stochastic trajectory modelling in the chaotic advection regime. *J. Fluid Mech.* **769**: 1–25.
- Gardiner CW. 2009. *Stochastic Methods: A Handbook for the Natural and Social Sciences* (4th edn). Springer: Berlin.
- Grassberger P. 2002. Go with the winners: A general Monte-Carlo strategy. *Comput. Phys. Commun.* **147**: 64–70.
- Hanna SR. 1982. Applications in air pollution modeling. In *Atmospheric Turbulence and Air Pollution Modeling*, Nieuwstadt FTM, van Dop H. (eds.): 275–310. D. Reidel Publishing: Dordrecht, Netherlands.
- Haynes PH, Vanneste J. 2014. Dispersion in the large-deviation regime. Part I: Shear flows and periodic flows. *J. Fluid Mech.* **745**: 321–350.
- Jones AR, Thomson DJ, Hort M, Devenish B. 2007. The UK Met Office’s next-generation atmospheric dispersion model, NAME III. In *Air Pollution Modeling and its Application XVII* (Proceedings of the 27th NATO/CCMS International Technical Meeting on Air Pollution Modelling and its Application), Borrego C, Norman AL. (eds.): 580–589. Springer: Berlin.
- Kemp JR, Thomson DJ. 1996. Dispersion in stable boundary layers using large-eddy simulation. *Atmos. Environ.* **30**: 2911–2923.
- Legg BJ, Raupach MR. 1982. Markov-chain simulation of particle dispersion in inhomogeneous flows: The mean drift velocity induced by a gradient in Eulerian velocity variance. *Boundary-Layer Meteorol.* **24**: 3–13.
- Lehoucq RB, Sorensen D, Yang C. 1998. *Arpack Users’ Guide: Solution of Large-scale Eigenvalue Problems with Implicitly Restarted Arnoldi Methods*. SIAM Publications: Philadelphia, PA.
- Majda AJ, Kramer PR. 1999. Simplified models for turbulent diffusion: Theory, numerical modelling and physical phenomena. *Phys. Rep.* **314**: 237–574.
- Ramli HM. 2016. ‘Stochastic trajectory modelling of atmospheric dispersion’, PhD thesis. University College: London.
- Ramli HM, Esler JG. 2016. Quantitative evaluation of numerical integration schemes for Lagrangian particle dispersion models. *Geosci. Model Dev.* **9**: 2441–2457.

- Pavliotis GA, Stuart AM. 2008. *Multiscale Methods Averaging and Homogenization*. Springer: New York, NY.
- Rodean HC. 1996. *Stochastic Lagrangian Models of Turbulent Diffusion*. Meteorological Monographs, Vol. 48. American Meteorological Society: Boston.
- Saffman PG. 1962. The effect of wind shear on horizontal spread from an instantaneous ground source. *Q. J. R. Meteorol. Soc.* **88**: 382–393.
- Smith FB. 1965. Role of wind shear in horizontal diffusion of ambient particles. *Q. J. R. Meteorol. Soc.* **91**: 318–329.
- Smith R. 2005. An analytical approach to shear dispersion and tracer age. *Boundary-Layer Meteorol.* **117**: 383–415.
- Stohl A, Forster C, Frank A, Seibert P, Wotawa G. 2005. Technical note: The Lagrangian particle dispersion model FLEXPART version 6.2. *Atmos. Chem. Phys.* **5**: 2461–2474.
- Taylor AD. 1982. Puff growth in an Ekman layer. *J. Atmos. Sci.* **39**: 837–850.
- Taylor GI. 1953. Dispersion of soluble matter in solvent flowing slowly through a tube. *Proc. R. Soc. London, Ser. A* **219**: 186–203.
- Thomson DJ. 1987. Criteria for the selection of stochastic models of particle trajectories in turbulent flows. *J. Fluid Mech.* **180**: 529–556.
- Thomson DJ, Physick WL, Maryon RH. 1997. Treatment of interfaces in random walk dispersion models. *J. Appl. Meteorol.* **36**: 1284–1295.
- Tyldesley JB, Wallington CE. 1965. Effect of wind shear and vertical diffusion on horizontal dispersion. *Q. J. R. Meteorol. Soc.* **91**: 158–174.
- Wilson JD, Flesch TK. 1993. Flow boundaries in random flight dispersion models: Enforcing the well-mixed condition. *J. Appl. Meteorol.* **32**: 1695–1707.
- Young WR, Jones S. 1991. Shear dispersion. *Phys. Fluids* **A3**: 1087–1101.